Table 3
Comparison of the performance for $Q1/P0$ with SUPG stabilization technique

Mesh	nz(ILU)	#neg	#itr.	S-time	I-time	T-time
ILU-VP(0)						
C	278766	42	N.G.	0.08	-	-
M	788937	80	N.G.	0.26	-	-
F	1690930	81	N.G.	0.63	-	-
ILU-VP(1)						
C	491594	49	N.G.	0.51	-	
M	1456137	8	152	1.60	5.10	6.70
F	3194066	4	155	4.18	12.24	16.42
ILU-VP(0) without SUPG in preconditioner						
C	278766	0	165	0.09	1.15	1.24
M	788937	0	556	0.25	11.41	11.66
F	1690930	0	889	0.63	41.92	42.55
ILU-VP(1) without SUPG in preconditioner						
C	491594	0	54	0.51	0.58	1.09
M	1456137	0	100	1.57	3.18	4.75
F	3194066	0	135	4.09	10.44	14.53

Mesh	#outer	#inner	S-time	I-time	T-time
SGS-Schur ($m_{in} = 5$)					
C	47	235	0.05	1.04	1.09
M	81	405	0.22	5.71	5.93
F	82	410	0.52	12.60	12.12
SGS-Schur ($m_{in} = 10$)					
C	41	407	0.05	1.45	1.50
M	50	500	0.21	5.19	5.40
F	53	530	0.52	12.00	12.52

The columns in the tables have the same meanings as those in Table 2. The process is terminated and denoted by "N.G." if it does not converge after 1000 iterations. "ILU-VP without SUPG in Preconditioner" means that the SUPG terms are not included in the construction of the preconditioner.

ILU based approach for this finite element discretization is feasible only if the ILU-VP(0) is successful. This, however, is not the case in our example. The increase in the number of iterations for SGS-Schur is of sub-linear order while it seems to be linear for ILU-VP(1). Thus, SGS-Schur seems highly preferable over ILU-VP for this discretization.

In Fig. 3, the convergence histories for the fine mesh are depicted for ILU-VP(1) and SGS-Schur with $m_{\text{in}} = 5$. Some stagnation of convergence in the intermediate stage is observed for ILU-VP(1). The ranges of such stagnation seem to be smaller for SGS-Schur than for ILU-VP(1). In particular, a satisfactory reduction rate of the residual norm is observed in the whole iterative process for $Q1/Q1$ with PSPG. This is a desirable behavior for a scalable iterative solution method.

7. Effects of the Krylov subspace method

In this section, we examine how the Krylov subspace method contributes to the convergence behavior of our methods. To this end we will observe the eigenvalue distributions of the Hessenberg matrices defined in Eq. (27). First, let us examine the influence of the chosen Krylov subspace method to weakly coupled

Table 4
Comparison of the performance of $Q1/Q1$ with SUPG and PSPG stabilization techniques

Mesh	nz(ILU)	zneg	zitr.	*S*-time	*I*-time	*T*-time
ILU-VP(0)						
C	441741	202	N.G.	0.29	-	-
M	1242430	434	N.G.	0.87	-	-
F	2650623	786	N.G.	1.97	-	-
ILU-VP(1)						
C	877717	0	75	2.30	1.24	3.54
M	2610806	0	110	8.62	6.38	15.00
F	5726559	0	147	17.97	16.92	34.89

Mesh	zouter	zinner	*S*-time	*I*-time	*T*-time
SGS-Schur ($m_{in} = 5$)					
C	21	99	0.14	0.84	0.98
M	24	114	0.44	2.69	3.13
F	26	129	1.01	6.41	7.42
SGS-Schur ($m_{in} = 10$)					
C	18	140	0.15	0.93	1.08
M	20	176	0.45	3.36	3.81
F	21	196	1.00	7.95	8.95

The columns in the tables have the same meanings as those in Table 2. The process is terminated and denoted by "N.G." if it does not converge after 1000 iterations.

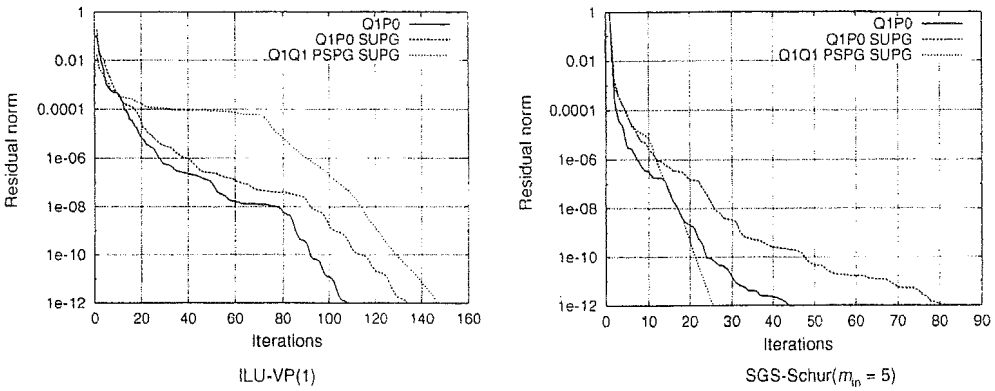

Fig. 3. Convergence histories.

approaches. Though this is not the main topic in the present paper, it is interesting to observe the instabilities of the approach and to see whether these instabilities can be eliminated by using Krylov subspace methods. We use the notations from Eq. (41). Then a Jacobi type weakly coupled approach for dealing with the coupling problem can be described as

$$\begin{cases} A_{ff}u_{f,k} = b_f - A_{fs}u_{s,k-1}, \\ A_{ss}u_{s,k} = b_s - A_{sf}u_{f,k-1}, \end{cases} \tag{45}$$

where $u_k = \begin{pmatrix} u_{f,k} \\ u_{s,k} \end{pmatrix}$ is the kth iterative solution, $b = \begin{pmatrix} b_f \\ b_s \end{pmatrix}$ the right-hand side. In this case, the fluid components and the structure components can be computed in parallel for each iteration. On the other hand, these components are computed in turn in the following Gauss–Seidel type approach:

$$\begin{cases} A_{ff}u_{f,k} = b_f - A_{fs}u_{s,k-1}, \\ A_{ss}u_{s,k} = b_s - A_{sf}u_{f,k}. \end{cases} \tag{46}$$

For both cases, the iteration process can be formulated as in Eq. (16) by putting

$$P_{Jac} = \begin{pmatrix} A_{ff} & 0 \\ 0 & A_{ss} \end{pmatrix} \quad \text{for the Jacobi type,} \tag{47}$$

$$P_{GS} = \begin{pmatrix} A_{ff} & 0 \\ A_{sf} & A_{ss} \end{pmatrix} \quad \text{for the Gauss Seidel type.} \tag{48}$$

In Table 5, the eigenvalues of the Hessenberg matrix minus the unit matrix are listed for the preconditioners defined by Eqs. (47) and (48). Here, the generation of the Krylov subspace in Eq. (25) is terminated when a convergence of $|r_k|/|b| \leqslant 10^{-12}$ is achieved with the GMRES iterations. The matrices are made of problems ($Q1/P0$ without stabilization, and $Q1/Q1$ with stabilization) on the coarse mesh in Section 6. In all cases, there are one or two extremely large eigenvalues that cause divergence of the simple iterative scheme described in Eq. (16). However, we can also see that the rest of the eigenvalues of $H(m)$ cluster

Table 5
The number of GMRES iterations performed to achieve the convergence (citr.) and the eigenvalue distribution of $H(m) - I$ where m is chosen as citr

citr.	Jacobi type 19	Gauss–Seidel type 8
Q1/P0C without SUPG in stabilization		
$\lambda_i - 1$	(0.149E−09, 0.522E+02)	(0.272E+04, 0.000E+00)
	(−0.320E−08, 0.270E+01)	(0.727E+01, 0.000E+00)
	(0.859E−02, 0.737E+00)	(0.506E−01, 0.000E+00)
	(0.219E−01, 0.582E+00)	(0.191E−01, 0.000E+00)
	(0.219E−01, 0.000E+00)	(−0.130E−03, 0.000E+00)
	(−0.200E−01, 0.000E+00)	(−0.671E−05, 0.000E+00)
	(−0.462E−03, 0.000E+00)	(0.811E−02, 0.000E+00)
	(0.103E−02, 0.996E−01)	(0.556E+00, 0.000E+00)
	(−0.383E−03, 0.162E+00)	
	(−0.906E−05, 0.225E+00)	
	(−0.599E−01, 0.437E+00)	
	11	6
Q1/Q1C with PSPG and SUPG		
$\lambda_i - 1$	(−0.561E−07, 0.522E+02)	(0.272E+04, 0.000E+00)
	(0.967E−05, 0.121E+00)	(0.146E−01, 0.000E+00)
	(−0.492E−03, 0.625E−01)	(−0.417E−03, 0.000E+00)
	(−0.421E−01, 0.000E+00)	(0.320E−04, 0.000E+00)
	(−0.130E−01, 0.000E+00)	(0.290E−02, 0.000E+00)
	(−0.128E−02, 0.000E+00)	(0.263E−02, 0.000E+00)
	(0.150E−01, 0.000E+00)	
	(0.651E−01, 0.000E+00)	

Since the eigenvalue distributions are symmetric for the real axis, only the eigenvalues in the upper half plane are listed.

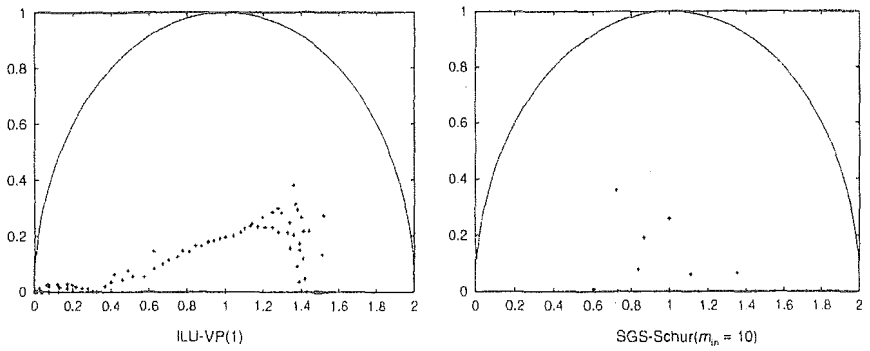

Fig. 4. The eigenvalue distributions of $H(m)$ in the upper half plane for $Q1/Q1F$. m is the number of GMRES iterations needed to achieve convergence. The unit circle at (0,1) is also depicted.

around (1,0). Thus, fast convergence was achieved for all cases with GMRES iteration. Another interesting fact is that we have similar extreme eigenvalues for both $Q1/P0$ and $Q1/Q1$, and that these change depending on the approaches.

Next, we observe the eigenvalue distributions of $H(m)$ (not of $H(m) - I$) for ILU-VP(1) and SGS-Schur-($m_{in} = 10$) for case $Q1/Q1$ on a fine mesh. In Fig. 4, the eigenvalues of $H(m)$ are plotted. For the SGS-Schur method, the extreme eigenvalue (0.295E+4,0) is not present in the figure. On the other hand, such an extreme eigenvalue is not produced by the ILU-VP(1) method. This may be due to the fact that the fluid–structure interaction is somehow well-approximated by the ILU factorization. We also note that the size of such extreme eigenmodes and the eigenvalues do not increase when we move from coarse to fine mesh. This is important for sustaining good convergence independent of mesh size. In both cases, the eigenvalues cluster around the real axis. Due to the good performance of the Schur complement approach for the fluid part, all eigenvalues, except the extreme one, are well bounded within the range [0.5, 1.7] for SGS-Schur. Thus, a good convergence result is obtained in spite of the existence of this extreme eigenvalue. On the other hand, we find some eigenvalues for ILU-VP(1) that are close to the origin, and the lower bound of the eigenvalue distributions approaches zero as the mesh gets finer. The presence of such eigenvalues is the main reason why the convergence of Krylov subspace methods slows down as the meshes get finer.

8. Conclusions

In this paper, we propose efficient and robust preconditioning methods based on ILU factorization and Schur complement techniques to accelerate the convergence of Krylov subspace iteration methods for solving strongly coupled fluid–structure interaction problems. It turns out in our numerical examples that the interaction of the fluid and the diaphragm can easily be dealt with by using a Krylov subspace method once robust preconditioners on both parts are defined. For the diaphragm part, sparse LU factorization is adopted which generates only a negligible overhead compared with the computation of the fluid part. Thus, our attention was directed to finding a good preconditioner for the fluid part. For the fluid part, convergence of the Krylov subspace methods is very sensitive to the accuracy of the approximation of the velocity–pressure and pressure–pressure coupling parts. For this reason, the ILU approach was not appropriate for the $Q1/Q1$ discretization due to the increase in fill-ins. We also observe that the Schur complement approach scales nicely with the size of the meshes used, especially for $Q1/Q1$ elements with the pressure stabilization technique PSPG.

Acknowledgement

We thank Mr. T. Sawada for his helpful support in preparing the data for the numerical experiments.

Appendix A. A preconditioner for the pressure part

Here, we will show some details of the preconditioner proposed in Section 4.2 for the Schur complement $S_{pp} = A_{pp} - A_{pv}P_{vv}^{-1}A_{vp}$ from Eq. (39). For simplicity, we assume that A_{vv} is symmetric positive-definite as in the case of the Stokes equation. Thus, P_{vv} is also symmetric positive-definite. Let us assume that A_{pp} is symmetric non-negative and that the following conditions hold on P_{pp}, A_{pv} and A_{vp}.

$$aM_{vv} \leqslant P_{vv} \leqslant bM_{vv}. \tag{A.1}$$

$$A_{pv} = -A_{vp}^{T} \tag{A.2}$$

for positive numbers a and b, and a positive matrix M_{vv}. Here, the inequality (A.1) means

$$a(v, M_{vv}v) \leqslant (v, P_{vv}v) \leqslant b(v, M_{vv}v), \quad \forall v \in V_h^l.$$

Under these assumptions, we obtain

$$A_{pp} - \frac{1}{b}A_{pv}M_{vv}^{-1}A_{vp} \leqslant S_{pp} \leqslant A_{pp} - \frac{1}{a}A_{pv}M_{vv}^{-1}A_{vp}.$$

Thus, if we take rowsum($|A_{vv}|$) as M_{vv} in Eq. (A.1), we obtain

$$\min\left(1, \frac{1}{b}\right)B_{2pp} \leqslant S_{pp} \leqslant \max\left(1, \frac{1}{a}\right)B_{2pp}.$$

with B_{2pp} in Eq. (40). The above estimates show that B_{2pp} is a good preconditioner if $\frac{b}{a}$ is well bounded.

In the case of PSPG, Eq. (A.2) is not fulfilled. Thus the above consideration is not valid if the stabilization yields a considerable change in A_{pv}. However, taking rowsum($|A_{vv}|$) as M_{vv} has the following advantage even in such a case. According to Eqs. (11), (12) and (14), the matrix with PSPG on the fluid part can be represented as

$$\begin{pmatrix} A_{vv} & A_{vp} \\ A_{pv} & A_{pp} \end{pmatrix} = \begin{pmatrix} M^{V} + \Delta t\gamma(A' + K) & -\Delta t\gamma G \\ M_\epsilon + \Delta t\gamma(G^{T} + A_\epsilon + K_\epsilon) & M^{P} + \Delta t\gamma(G_\epsilon + A^{P}) \end{pmatrix}.$$

Here, the matrices with ϵ stem from the PSPG stabilization. Thus, the matrix to be factorized for constructing the preconditioner to the Schur complement can be expressed as

$$A_{pp} - A_{pv}M_{vv}^{-1}A_{vp} = M^{P} + \Delta t\gamma A^{P} + \Delta t^2\gamma^2 G^{T}M_{vv}^{-1}G + \Delta t\gamma\{G_\epsilon + (M_\epsilon + \Delta t\gamma(A_\epsilon + K_\epsilon))M_{vv}^{-1}G\}.$$

In the above expression, the influence of PSPG is seen in the last term on the right-hand side:

$$C_{pp} = G_\epsilon + (M_\epsilon + \Delta t\gamma(A_\epsilon + K_\epsilon))M_{vv}^{-1}G.$$

To examine the stability of this term, let us represent the matrices arising from PSPG as follows:

$$G_\epsilon = \tau G^{T} * G, \quad M_\epsilon = -\tau G^{T} * M^{V}, \quad A_\epsilon = -\tau G^{T} * A', \quad K_\epsilon = -\tau G^{T} * K.$$

Here, τ is a positive function. The notation "$*$" indicates that the product of two operators is taken in the weak form, namely, before the integration for the matrix assembly takes place, the product of the two operators is taken. With this notation, we obtain

$$C_{pp} = \tau G^T * G - \tau\{G^T * (M^V + \Delta t\gamma(A' + K))\}M_{vv}^{-1}G.$$

Thus, if

$$A_{vv} = M^V + \Delta t\gamma(A' + K) \leqslant M_{vv}$$

is fulfilled, as for the choice $M_{vv} = \text{rowsum}(|A_{vv}|)$, the non-negativeness of C_{pp} can be assured. This contributes to the stability of the ILU factorization of B_{2pp} in Eq. (40).

Appendix B. Construction of the initial guess for the nearly singular linear system on the pressure part

If no boundary values are given for the pressure, the constant pressure vector spans the null space of the operator A_{vp} in Eq. (39). In this case, since the diagonal entries in A_{pp} are several orders of magnitudes smaller than the entries in $A_{pv}P_{vv}^{-1}A_{vp}$, it is likely that the condition number of S_{pp} in Eq. (39) is extremely large. Thus, the convergence of the inner iteration for the linear system with S_{pp} is very poor unless the errors in the null space are mostly removed. Let S be a positive symmetric square matrix and c be a given non-zero vector, and let the system to be solved be

$$Sp = b.$$

Then, for example, the minimization problem of the energy

$$E(p) = (Sp - b, S^{-1}(Sp - b))$$

in the one dimensional space spanned by c can be solved by determining the coefficient $\alpha(c)$ by

$$\alpha(c) = \frac{(b, c)}{(Sc, c)}.$$

Though, in our problem, S_{pp} in Eq. (39) is not exactly symmetric, we observe that the above choice works well for all the problems tested here. When the symmetry is totally broken, we suggest minimizing the squared residual norm:

$$\text{RES2}(p) = (Sp - b, Sp - b)$$

as an alternative choice. Then, the coefficient is obtained from

$$\alpha(c) = \frac{(b, Sc)}{(Sc, Sc)}.$$

References

[1] R. Benney, K. Stein, A computational fluid–structure interaction model for parachute inflation, J. Aircraft 33 (1996) 730–736.
[2] O. Dahl, S.O. Wille, An ILU preconditioner with coupled node fill-in for iterative solution of the mixed finite element methods and Navier Stokes equations, Int. J. Num. Methods Fluids 15 (1992) 525–544.
[3] E.N. Dvorkin, K.J. Bathe, A continum mechanics based four-node shell element for general nonlinear analysis, Engrg. Comput. 1 (1984) 77–88.
[4] T.J.R. Hughes, A.N. Brooks, A multi-dimensional upwind scheme with no crosswind diffusion, in: T.J.R. Hughes (Ed.), Finite Element Methods for Convection Dominated Flows, AMD-vol. 34, ASME, New York, 1979, pp. 19–35.

[5] T.J.R. Hughes, R.L. Taylor, W. Kanoknukulchai, A simple and efficient finite element for plate bending, Int. J. Num. Methods Engrg. 11 (1984) 1529–1543.
[6] Ilse C.F. Ipsen, A note on preconditioning nonsymmetric matrices, SIAM J. Sci. Comput. 23 (2001) 1050–1051.
[7] M.F. Murphy, G.H. Golub, A.J. Wathen, A note on preconditioning for indefinite linear systems, SIAM J. Sci. Comput. 21 (2000) 1969–1972.
[8] Y. Saad, Iterative Methods for Sparse Linear Systems, PWS Publishing Company, Boston, 1996.
[9] Y. Saad, M.H. Schultz, GMRES: a generalized minimal residual algorithm for solving nonsymmetric linear systems, SIAM J. Sci. Comput. 7 (1986) 856–869.
[10] Y. Saad, A flexible inner–outer preconditioned GMRES algorithm, SIAM J. Sci. Comput. 14 (1993) 461–469.
[11] A. Sameh, V. Sarin, Parallel algorithms for indefinite linear systems, Parall. Comput. 28 (2002) 285–299.
[12] A. Sameh, V. Sarin, Hybrid parallel linear solvers, Int. J. Comput. Fluid Dyn. 12 (1999) 213–223.
[13] G. Segal, K. Vuik, A simple iterative linear solver for the 3D incompressible Navier–Stokes equations discretized by the finite element method, Faculty of Technical Mathematics and Informatics, Delft University of Technology, 1995, TUD Report 95-37.
[14] K. Stein, Simulation and Modeling Techniques for Parachute Fluid–Structure Interactions, Ph.D. Thesis, University of Minnesota, 1996.
[15] T.E. Tezduyar, J. Liou, D.K. Ganjoo, Incompressible flow computations based on the vorticity-stream function and velocity-pressure formulations, Comput. Struct. 35 (1990) 445–472.
[16] T.E. Tezduyar, Stabilized finite element formulation for incompressible flow, Adv. Appl. Mech. 28 (1991) 1–44.
[17] Q. Zhang, T. Hisada, Analysis of fluid–structure interaction problems with structural buckling and large domain changes by ALE finite element method, Comput. Methods Appl. Mech. Engrg. 190 (2001) 6341–6357.

Further reading

[i] J.A. Meijerink, H.A. van der Vorst, An iterative solution method for linear systems of which the coefficient matrix is a symmetric M-matrix, Math. Comput. 31 (1997) 148–162.
[ii] J.A. Meijerink, H.A. van der Vorst, Guidelines for the usage of incomplete decompositions in solving sets of linear equations as they occur in practical problems, J. Comput. Phys. 11 (1981) 131–155.

Combined Effects of Nifekalant and Lidocaine on the Spiral-Type Re-Entry in a Perfused 2-Dimensional Layer of Rabbit Ventricular Myocardium

Mari Amino, MD; Masatoshi Yamazaki, MD; Harumichi Nakagawa, MD; Haruo Honjo, MD;
Yusuke Okuno; Koichiro Yoshioka, MD; Teruhisa Tanabe, MD;
Kenji Yasui, MD; Jong-Kook Lee, MD; Mitsuru Horiba, MD;
Kaichiro Kamiya, MD; Itsuo Kodama, MD

Circulation Journal
Vol. 69 No. 5 May 2005
(Pages 576–584)

Circ J 2005; **69:** 576–584

Combined Effects of Nifekalant and Lidocaine on the Spiral-Type Re-Entry in a Perfused 2-Dimensional Layer of Rabbit Ventricular Myocardium

Mari Amino, MD; Masatoshi Yamazaki, MD*; Harumichi Nakagawa, MD*; Haruo Honjo, MD*; Yusuke Okuno*; Koichiro Yoshioka, MD; Teruhisa Tanabe, MD; Kenji Yasui, MD*; Jong-Kook Lee, MD*; Mitsuru Horiba, MD*; Kaichiro Kamiya, MD*; Itsuo Kodama, MD*

Background Spiral re-entry plays the principal role in the genesis of ventricular tachycardia and ventricular fibrillation (VT/VF). The specific I_{Kr} blocker, nifekakant (NIF) has, often in combination with lidocaine (LID), recently been used in Japan to prevent recurrent VT/VF, but the combined effects of these drugs on spiral re-entry had never been investigated.

Methods and Results A ventricular epicardial sheet was obtained from 13 Langendorff-perfused rabbit hearts by means of a cryoprocedure, and epicardial excitations were analyzed with a high-resolution optical mapping system. Nifekakant (0.5 μmol/L) caused significant prolongation of action potential duration (APD) and LID (3 μmol/L) attenuated the APD prolongation without affecting the conduction velocity. VT were induced in 6 hearts by cross-field stimulation, and single- or double-loop spirals circulating around variable functional block lines were visualized during the VT. Nifekakant reduced VT cycle length and caused early termination in association with destabilization of the spiral dynamics (prolongation of functional block line, frequent local conduction block, and extensive meandering). These modifications of spiral-type re-entrant VT by NIF were prevented by addition of LID.

Conclusions The effects of NIF on the spiral excitations are reversed by LID. This interaction should be taken into account when these drugs are used in combination to treat VT/VF. (*Circ J* 2005; **69:** 576–584)

Key Words: Lidocaine; Nifekalant; Optical mapping; Spiral re-entry; Ventricular tachycardia

Spiral-type excitation is the principal mechanism of functional re-entry for the genesis of life-threatening ventricular tachycardia and ventricular fibrillation (VT/VF).[1,2] Nifekalant (NIF) hydrochloride is a new class III antiarrhythmic drug developed in Japan that causes dose-dependent prolongation of action potential duration (APD) in both atrial and ventricular muscle, mainly by reducing the rapid component of the delayed rectifier potassium current (I_{Kr}).[3–7] The 2000 American Heart Association Guidelines for cardiopulmonary resuscitation (CPR) recommends intravenous amiodarone to prevent recurrent VT/VF,[8,9] but amiodarone has not yet been approved for CPR in Japan and intravenous NIF is used, often in combination with lidocaine (LID), as an alternative.[10] Nifekakant and LID are also used sequentially to treat recurrent VT/VF resistant to DC shocks;[11–13] however, little information is available on the electropharmacological basis for the combined use of these drugs. The present study was designed to investigate the effects of NIF and NIF+LID on the spiral-type excitation in a perfused 2-dimensional (D) layer of rabbit ventricle by using our custom-made high-resolution optical mapping system.

(Received September 3, 2004; revised manuscript received January 27, 2005; accepted February 15, 2005)

*Department of Cardiology, Tokai University School of Medicine, Shimokasuya, Isehara, *Research Institute of Environmental Medicine, Nagoya University, Nagoya, Japan*

Mailing address: Mari Amino, MD, Department of Cardiology, Tokai University School of Medicine, 143 Shimokasuya, Isehara 259-1193, Japan. E-mail: mariam@is.icc.u-tokai.ac.jp

Methods

Experimental Model

Japanese White rabbits of both sexes weighing 1.7–2.0 kg (n=13) were anesthetized with thiamylal sodium (10–15 mg/kg), and after opening the thorax, the heart was rapidly removed. Complete atrioventricular block was produced by ligating the His bundle with fine silk thread. The aorta was then cannulated, and the heart was connected to a Langendorff perfusion apparatus. The coronary arteries were perfused with modified Krebs Ringer solution at a constant flow (35–45 ml/min). The solution was equilibrated with 95% O_2 and 5% CO_2 to maintain its pH at 7.4, and its temperature was maintained at 35°C.

Because of its 3-D structure with variable filament configuration, vortex-type excitations appear only transiently and incidentally in the intact heart,[14] thereby hampering detailed analysis of spiral dynamics by optical mapping. To avoid this problem, we created a 2-D preparation by the method described by Schalij et al.[15] In brief, the Langendorff-perfused rabbit heart was immersed in a tissue bath containing perfusion fluid at 35°C, and a cryoprobe made of copper was inserted into the left ventricular cavity, and the probe was then filled with liquid nitrogen (–192°C) for 5 min. This freezing procedure destroyed the endocardial and intramural layers of the free wall of the left ventricle and the total interventricular septum, leaving only

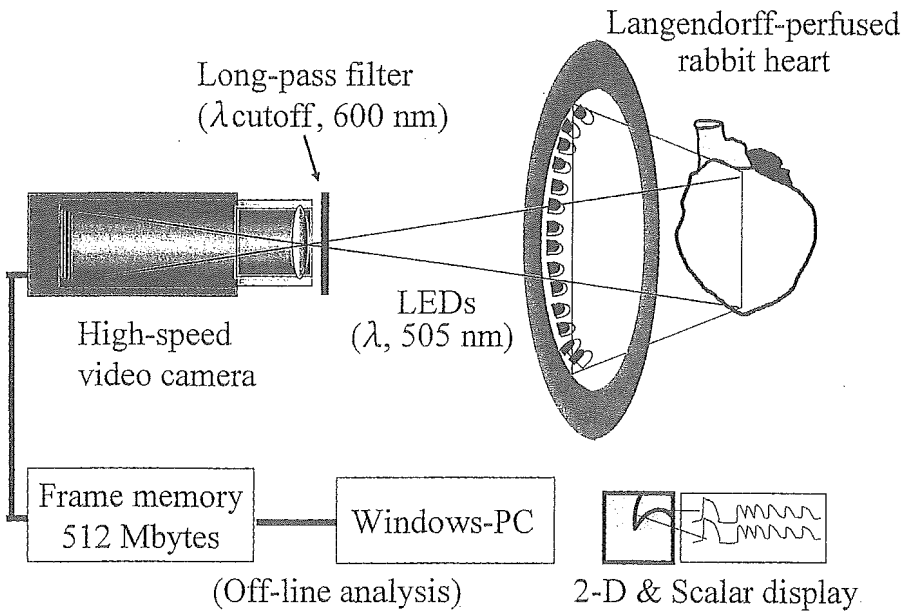

Fig 1. Experimental set-up for optical mapping. The Langendorff-perfused rabbit heart was stained with a voltage-sensitive dye, di-4-ANEPPS, and illuminated with bluish-green light-emitting diodes (LED) mounted on a ring-shaped bracket. The peak wave length (λ) of the excitation light was 505 nm. The fluorescence signals emitted from the surface of the heart were recorded with a high-speed digital video camera (Fastcam-Ultima 40k, Photron) through a long pass filter (cut-off wavelength of 600 nm). The digital images were stored temporarily in the frame memory (512 megabytes), and transferred to a Windows-based personal computer for off-line analysis in 2-D and scalar display.

a thin left ventricular epicardial layer intact. At the end of the experiment the heart was stained with 2,3,5,-triphenyltetrazolium chloride (TTC) and sectioned parallel to the atrioventricular ring from the base to the apex at 2-mm intervals. The thickness of surviving myocardium that stained deeply with TTC (preservation of dehydrogenase activity) was 1.0±0.3 mm (6 hearts).

High-Resolution Optical Mapping

After endocardial freezing the hearts were stained for 10 min with the voltage-sensitive dye di-4-ANEPPS (Molecular Probes), at 2 μmol/L, added to the perfusate. This initial loading was followed by continuous application of 0.2 μmol/L di-4-ANEPPS for 120–150 min during the rest of the experiments. To minimize motion artifacts, 15 mmol/L 2,3-butandione monoxime (BDM, Sigma, St Louis, MO, USA) was added to the perfusate.

Fig 1 is a schematic diagram of the optical signal recording system. The vertically hanging heart placed in the Langendorff apparatus was illuminated with bluish-green light-emitting diodes (LED). The LED (222 elements in all; NSPE 500S, Nichia) were mounted on a ring-shaped bracket placed in front of the heart. The peak wave length (λ) of the excitation light was 505 nm with a half bandwidth ($\Delta\lambda$) of ~20 nm. The fluorescence emitted from the epicardial surface of the heart was recorded by a high-speed digital video camera (Fastcam-Ultima 40K, Photron). This solid-state image sensing device camera was used to acquire 8-bit gray scale images from 256×256 sites simultaneously at a speed of 750 frames/s (sampling interval at 1.33 ms). A Micro Nikkor lens (105 mm, f/2.8D, Nikon) with long-pass glass filter (cut-off wavelength 600 nm, R60, Nikon) was mounted on the video camera. The images acquired (30× 30 mm) covered the antero-lateral surface of the left ventricle and part of the anterior surface of the right ventricle, yielding a spatial resolution at 0.12 mm per pixel. Each acquisition lasted 10.9 s. The digital images were stored temporarily in the frame memory of the video camera system (512 M bytes, 8,192 frames), and then transferred to a Windows-based personal computer for off-line analysis.

Signal Processing

The background fluorescence was subtracted from each frame to reveal the signal. Because of the relatively large background fluorescence, the dynamic range of fluorescence change for each electrical excitation was 12–23 gray levels. The fluorescence signals were inverted and then spatially averaged to reduce noise. The data from 3×3 pixels were averaged at the respective recording site to obtain isochrone maps, whereas the data from 4×4 pixels were averaged to analyze action potential configuration. Spatial resolution after this low-pass filtering was 0.36–0.48 mm.

Isochrone maps were generated from the filtered video imaging data by analyzing the value of each pixel over time. A point in each time series was labeled as part of a wave front, if the first derivative of fluorescence was >30% of the peak value in the respective 100–500 frames sampled. This helped to eliminate most maxima because of noise. The leading edge was identified as the activation wave front from the data points forming a band.

To analyze action potential configuration, a 5-point time median filter was applied to the spatially averaged data, and then the data were normalized to within the range of the maximum and the minimum values in the respective 700–1,000 frames sampled.[16] A time point at 10% depolarization in the upstroke phase and a time point at 90% repolarization in its repolarization phase were identified for each action potential signal, and their interval was measured as APD at 90% repolarization (APD_{90}). The distribution of APD_{90} values in the recording area was displayed as color gradient maps with 1.33 ms steps ranging from red (the shortest) to blue (the longest).

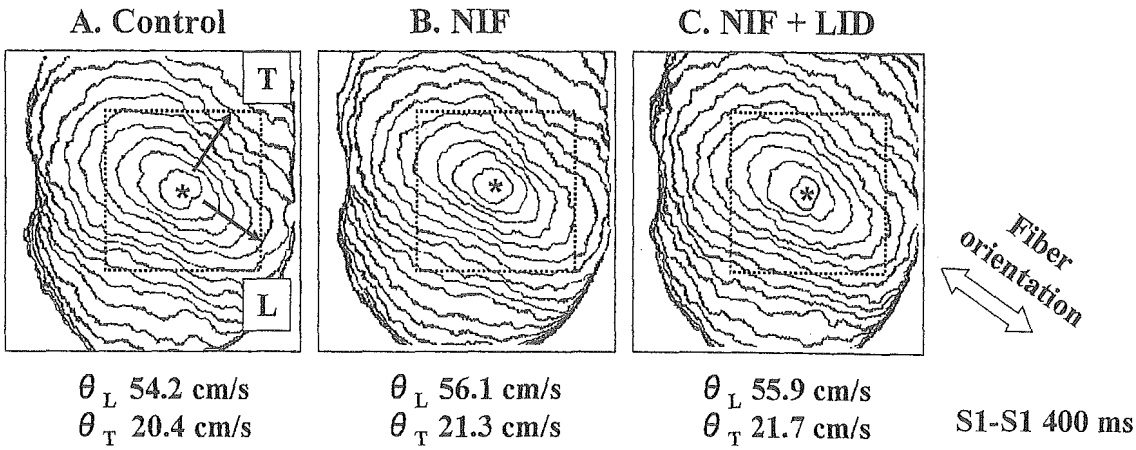

Fig 2. Isochrone maps of activation during constant stimulation at the center (*) of the left ventricular free wall at a cycle length of 400 ms. Fiber orientation is indicated by the arrow. Isochrones were drawn automatically every 4 ms with our custom-made software. Data were obtained from the same rabbit heart before (control) and 30 min after application of 0.5 μmol/L nifekalant (NIF), and 10 min after addition of 3 μmol/L lidocaine (NIF+LID). Conduction velocities in longitudinal (θL) and transverse (θT) directions were measured in a central 15×15 mm square (dotted line) around the stimulation site.

Experimental Protocols

Conduction velocity (CV) and APD90 were measured during constant stimulation (S1) from the center of the left ventricular free wall at a cycle length (CL) of 250 ms and 400 ms. A monopolar electrode made of platinum wires was used for stimulation. The pulses applied were 2 ms in duration and had an intensity twice the diastolic threshold. Longitudinal (L) and transverse (T) directions of propagation were determined from the activation maps elicited by S1 stimulation. A line for L propagation was drawn from the pacing site to the outer area of the map, so that it crossed the most widely spaced isochrones (Fig 2A). A second line for T propagation was drawn perpendicular to the first line through the densely spaced isochrones. The CV was measured in a central 15×15 mm square around the stimulation site, as measurement in the outer periphery would be hampered by the sharp curvature of the ventricular surface. The CV in the L and T directions were calculated from the slope of a linear least-square fit of the activation time plotted against the distance. Data from an area very close to the stimulation site (<2 mm) were excluded to minimize the virtual electrode polarization effects.

In experiments to induce VT resulting from spiral-type excitation, 18 S1 stimuli at a CL of 400 ms were applied to the apex through a pair of contiguous bipolor electrodes. A 10 ms DC stimulus (S2, monophasic pulse at 20 V) was then delivered through Ag–AgCl paddle electrodes (5 mm diameter) placed on the lateral surface of the both ventricles. This cross-field S2 stimulation was applied during the vulnerable window of the last S1 excitation. When sustained VTs >30 s were induced, a salvage DC shock (10 ms monophasic pulse at 60–80 V) was applied to terminate the arrhythmia.

Data were obtained before (baseline) and 30 min after application of 0.5 μmol/L NIF, 10 min after addition of 3 μmol/L LID, and 15 min after washing the LID out.

At the end of experiment the tissue in 2 preparations was fixed in 10% formalin and sectioned parallel to the epicardium at 100 μm intervals. The sections were stained with hematoxylin and eosin to examine the fiber orientation in the mapped area.

Statistical Analysis

Group data were expressed as mean values ± SE. Statistical comparisons were performed by two-way or one-way analysis of variance (ANOVA with Fisher) when appropriate. Differences were considered significant when the p-value was <0.05.

Results

Conduction Velocity and Action Potential Configuration

Fig 2A shows activation sequences during constant stimulation from the anterior center of the left ventricular free wall (S1–S1 400 ms). At the highest speed the activation front proceeded centrifugally along an oblique line in the left upper and right lower directions, and in directions perpendicular to the line at the slowest speed. As a result, the isochrones of activation showed a smooth and symmetric elliptical pattern. In the rabbit, the long axis of the ellipse has been found to correspond to the fiber orientation of subepicardial cardiac muscle in the anterior left ventricular free wall.[15] In 2 hearts we confirmed that the fiber orientation correlated well with the electrical axis of fast conduction. In the central 15×15 mm square (dotted line), there was a linear relationship between activation times and distances from the stimulation site in either L or T direction. The CV (θL and θT) and their anisotropic ratio (θL/θT) were calculated from the slopes.

Application of 0.5 μmol/L NIF alone for 20 min and addition of 3 μmol/L LID for 10 min (NIF+LID) produced no appreciable changes in the uniform anisotropic conduction property (Fig 2B,C). The results obtained from 6 hearts at S1–S1 400 ms and 250 ms are summarized in Table 1. There were no significant differences at either long or short basic CL in θL, θT, or θL/θT among the control, NIF, and NIF+LID conditions.

Fig 3 shows representative changes in APD in response to drug application. Left panels are color maps of APD90 during basic stimulation at the anterior center of the left ventricular free wall. The APD90 values in the entire mapping area are displayed as color gradients; the shortest APD90 is colored red, and the longest, blue. Right traces show optical action potential signals recorded from 4 sites

Table 1 Effects of Nifekalant and Lidocaine on Conduction Velocity During Longitudinal and Transverse Propagation During Constant Stimulation

	n	θ_L (cm/s)	θ_T (cm/s)	θ_L/θ_T
S1-S1 400 ms				
Control	6	55.1±2.7	22.2±1.5	2.53±0.16
NIF	6	56.9±2.2	22.5±0.8	2.53±0.07
NIF + LID	6	57.9±3.0	22.4±1.5	2.60±0.09
LID wash	6	57.1±3.3	23.3±0.8	2.40±0.15
S1-S1 250 ms				
Control	6	54.4±3.0	19.7±1.4	2.80±0.20
NIF	6	55.3±2.0	21.2±1.1	2.64±0.11
NIF + LID	6	55.8±3.6	21.1±1.6	2.76±0.06
LID wash	6	55.4±2.7	21.0±1.6	2.68±0.17

Values are means±SE of 6 experiments each. θ_L and θ_T: conduction velocity during longitudinal propagation and transverse propagation, respectively. θ_L/θ_T: anisotropic ratio of the conduction velocity. Data were obtained before (Control) and 30 min after application of 0.5 μmol/L nifekalant (NIF), 10 min after addition of 3 μmol/L lodocaine (NIF + LID), and 15 min after washing lodocaine out (LID wash). The hearts were stimulated at a cycle length of either 400 ms or 250 ms.

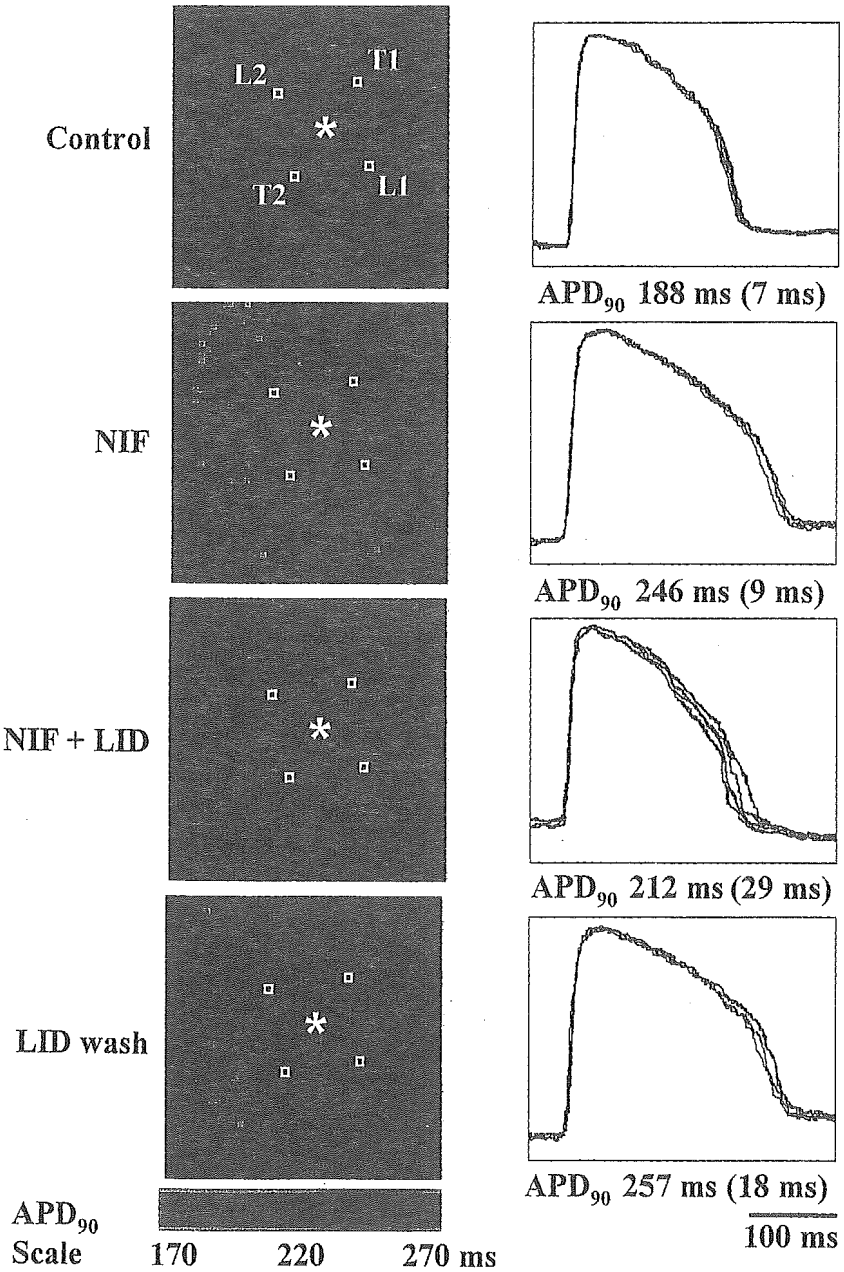

Fig 3. Changes in action potential duration (APD) in response to drug application. Left: color-coded maps of APD90 in the recording area were displayed as color gradients in 1.33 ms steps, ranging from red (shortest) to blue (longest). The records were obtained during a constant stimulation at the center (*) of the left ventricular free wall at a cycle length of 400 ms in a heart before (control) and 30 min after application of 0.5 μmol/L nifekalant (NIF), 10 min after addition of 3 μmol/L lidocaine (NIF + LID), and 15 min after washing lidocaine out (LID wash). The traces at the right show optical action potential signals recorded from 4 sites 5 mm away from the stimulation site in the direction of L and T propagation (L1, L2, T1, T2). Averaged APD90 values at the 4 sites and their variation (dispersion) are shown at the bottom. The almost uniform prolongation of APD90 by NIF was partially reversed by addition of LID, and this LID action was abolished after washing out the drug.

Table 2 Effects of Nifekalant and Lidocaine on the Action Potential Duration (APD) and Its Dispersion (APDD) During Constant Stimulation

	n	APD_{90} (ms) [S1-S1 400 ms]	APD_{90} (ms) [S1-S1 250 ms]	APDD (ms) [S1-S1 400 ms]	APDD (ms) [S1-S1 250 ms]
Control	6	187±8	136±5	12±1	13±2
NIF	6	255±5*	154±5*	13±2	14±2
NIF+LID	6	220±7*,#	149±6	28±3*,#	21±2*,#
LID wash	6	268±8*	167±7*	20±2	16±2

*Values are means±SE of 6 experiments each. Action potential duration at 90% repolarization (APD_{90}) was measured at 4 sites 5 mm from the stimulation site in the direction of logitudinal (L) and transverse (T) propagation (L1, L2, T1, T2 as shown in Fig 3), and the 4 values for each heart were averaged. APD dispersion (APPD) in each heart was obtained from the maximum difference in APD_{90} among the 4 values (L1, L2, T1, T2). Data were obtained before (Control) and 30 min after application of 0.5 μmol/L nifekalant (NIF), 10 min after addition of 3 μmol/L lidocaine (NIF+LID), and 15 min after washing lidocaine out (LID wash). The hearts were stimulated at a cycle length of either 400 ms or 250 ms. *Significantly different from the control at $p<0.01$. #Significantly different from NIF alone at $p<0.05$.*

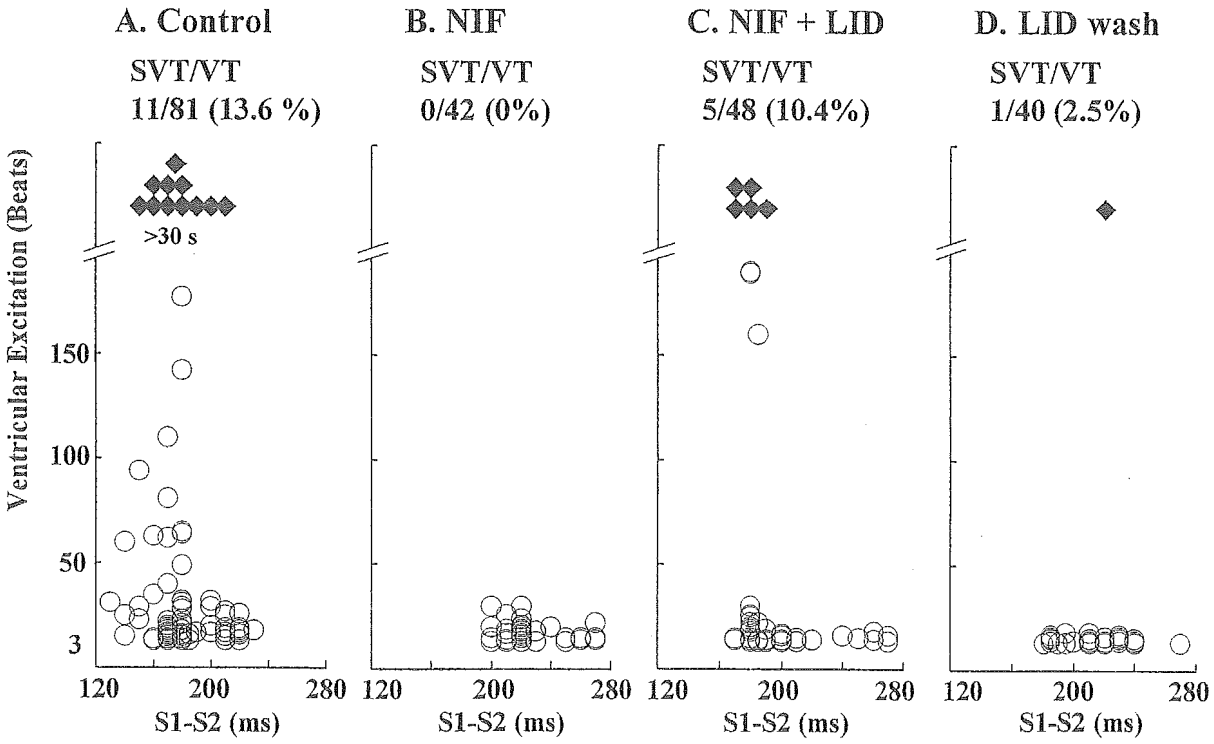

Fig 4. Vulnerability to ventricular tachycardia (VT) induction by cross-field stimulation. Abscissas: S1–S2 coupling interval. Ordinates: Beat count of the VT induced. Ventricular tachycardia lasting >30 s were defined as the sustained type (diamonds), whereas those terminating within 30 s were defined as the non-sustained type (open circles). The ratio of sustained VT episodes to all VT episodes is shown at the top (SVT/VT). Data were obtained before (A: control) and 30–35 min after single application of 0.5 μmol/L nifekant (B: NIF), 10–15 min after addition of 3 μmol/L lidocaine (C: NIF+LID), and 15–20 min after washing lidocaine out (D: 10 min, LID wash). Ventricular tachycardia induced after exposure to NIF alone were terminated much earlier than in the control (no SVT). This NIF action was partially prevented by LID, and the LID action was reversible.

5 mm from the stimulation site in direction of L and T propagation (L1, L2, T1, T2). The average APD_{90} value at the 4 sites and its variation (dispersion) are shown at the bottom. All the data in Fig 3 were obtained from the same heart.

Application of NIF alone caused an almost uniform prolongation of APD_{90}. The average value at the 4 sites increased from 188 ms to 246 ms, but its dispersion was unaffected (7 ms and 9 ms, respectively). The APD prolongation was partially reversed after addition of LID. In the presence of NIF+LID, the average APD_{90} value returned to 212 ms, but its dispersion was increased to 29 ms. Washout of LID for 20 min resulted in longer APD in the entire area mapped; the average APD_{90} value at the 4 sites (257 ms) was comparable to the value after application of NIF alone. The dispersion of APD_{90} was reduced to 18 ms.

The results obtained from 6 hearts at S1–S1 400 ms and 250 ms are summarized in Table 2. At the longer CL (S1–S1 400 ms), application of NIF alone resulted in a significant increase in APD_{90} (by 36.6±6.8%) without affecting its dispersion. Addition of LID resulted in significant shortening of APD_{90} (by 14.0±6.4%) and a significant increase in dispersion. After washing out LID, the APD_{90} and its dispersion returned toward the values after application of NIF alone. Similar but less marked changes in APD_{90} were induced by application of NIF and LID at the shorter CL (S1–S1 250 ms).

Induction of VT by Cross-Field Stimulation

VTs were induced in 6 hearts by S2 cross-field stimulation applied during the vulnerable window of S1 excitation. VTs were polymorphic during the first several beats, but became more stable during the subsequent beats and had an almost monomorphic configuration. Under the drug-free control conditions (control), 81 VT were induced in the S1–S2 interval (vulnerable window) of 130–230 ms. Seventy of the 81 VT terminated spontaneously (non-sustained), whereas the remaining 11 persisted for >30 s (sustained); the incidence of sustained VT was 13.6% (Fig 4A). After application of NIF alone (0.5 μmol/L), VT could also be induced with longer S1–S2 intervals (200–270 ms), but they terminated earlier than under control conditions (Fig 4B). In the presence of NIF alone, all 42 VT terminated spontaneously within 20 beats (non-sustained VT).

Table 3 Effects of Nifekalant and Lidocaine on the Duration and Cycle Length of Non-Sustained Ventricular Tachycardia (NSVT) Induced by S1-S2 Cross-Field Stimulation

	n	*VT duration (s)*	*VTCL (ms)*
Control	*70*	*3.1±0.5*	*158±2*
NIF	*42*	*1.5±0.1**	*200±5**
NIF + LID	*43*	*2.4±0.9#*	*173±3*,#*
LID wash	*39*	*0.8±0.1**	*193±7**

*Values are means ± SE of 39–70 episodes of NSVT induced in 6 hearts. Data were obtained before (Control) and 30 min after application of 0.5 μmol/L nifekalant (NIF), 10 min after addition of 3 μmol/L lidocaine (NIF + LID), and 15 min after washing lodocaine out (LID wash). Ventricular tachycardias (VTs) were induced by S1-S2 cross-field stimulation. *Significantly different from control at $p<0.01$. #Significantly different from NIF alone at $p<0.05$.*

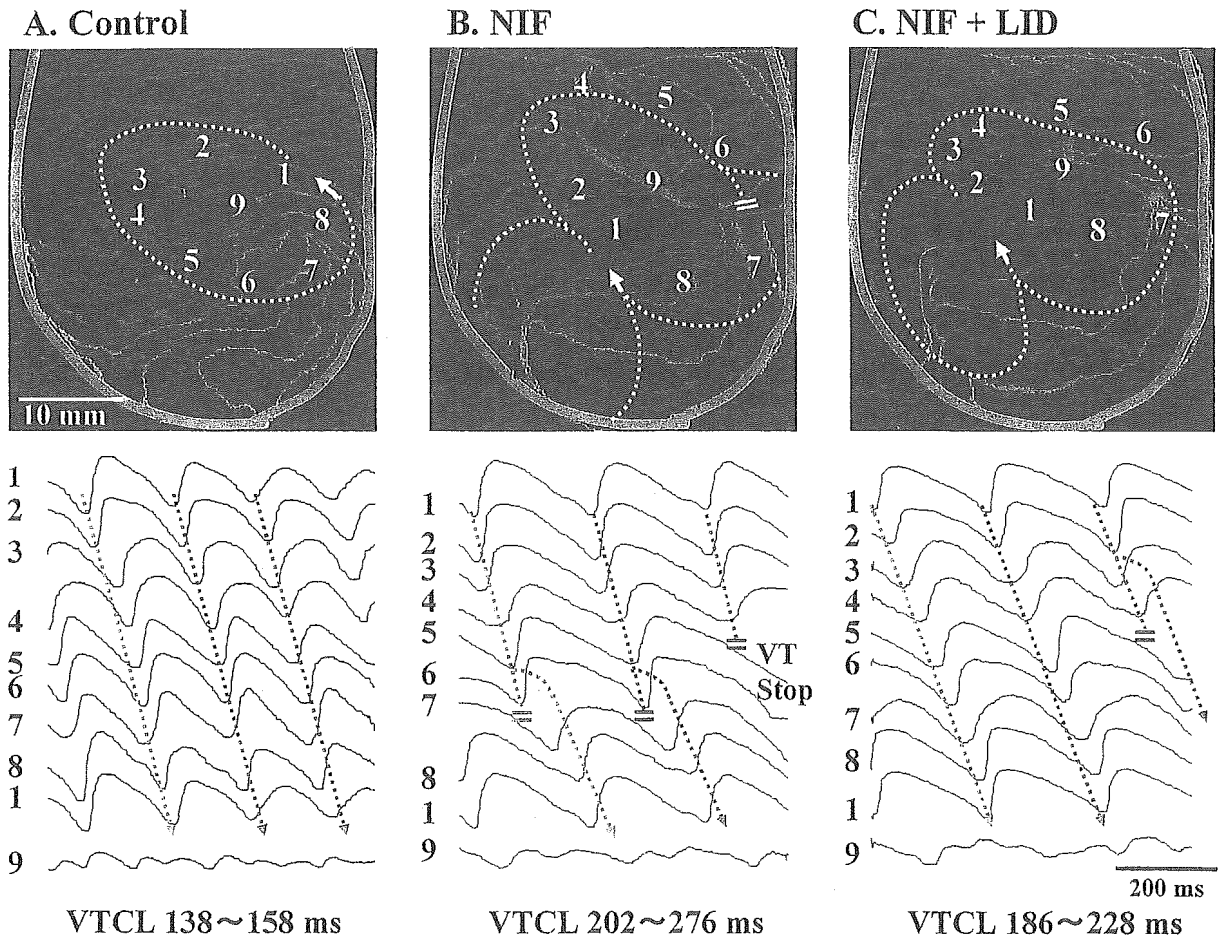

Fig 5. Modification of spiral dynamics by nifekalant and lidocaine. (Upper panels) isochrone maps of activation during ventricular tachycardias (VT) induced by cross-field stimulation before drug application (A: control), 30 min after application of 0.5 μmol/L nifekalant (B: NIF), and 10 min after addition of 3 μmol/L lidocaine (C: NIF+LID). The data were obtained from the same heart. The isochrones (green lines for the earlier wave fronts, and blue lines for the later wave fronts) were drawn every 4 ms. Thick red lines indicate functional block lines. (Lower panels) Sequential records of optical action potential signals from 9 sites indicated on the respective isochrone map. The cycle of excitation corresponding to the isochrone map (Top) is indicated by the dotted red line, and the next 2 cycles are indicated by dotted blue lines. The cycle length of ventricular excitation (VTCL) of the isochrone map (the cycle indicated by red dotted line in the lower panel) is shown at the bottom. A (control): an almost stable single-loop circuit around a line of functional block is repeated during the VT lasting >30 s. B (NIF): unstable (large meandering) double-loop (figure-8) circuits circulating around 2 lines of functional block are characterized by frequent localized conduction block, giving rise to a shift of the circuits. Ventricular tachycardia terminated within 2 s (third cycle in the lower panel). C (NIF+LID): more stable (little meandering) double-loop (figure-8) circuits circulating around 2 lines of functional block are seen during VT lasting 11 s. Localized conduction block causing a shift of the circuit (third cycle in the lower panel) was less frequent than with NIF alone.

After addition of LID (NIF+LID) the vulnerable window became wider (S1–S2 interval of 170–270 ms), and the VT induced lasted longer than after exposure to NIF alone (Fig 4C). The incidence of sustained VT increased to 5/48 (10.4%). When LID was washed out (LID wash), the vulnerable window shifted again to a similar range as obtained with NIF alone (S1–S2 interval of 180–270 ms), and most of the VT (39/40) terminated spontaneously within 7 beats (Fig 4D).

Table 3 summarizes the CL and the duration of non-sustained VT in the 6 hearts. The non-sustained VT induced in the hearts after exposure to NIF alone were characterized by a significantly longer CL (by 27.1%) and a significantly shorter duration (by 53.7%) than induced under the control conditions. The non-sustained VT induced after additions of LID (NIF+LID) were of significantly longer duration and significantly shorter CL than those induced with NIF alone. The VT with NIF+LID had slightly longer CL than in the controls, but there was no significant difference in VT duration between the 2 groups. Wash-out of LID resulted in a resumption of much shorter duration and much longer CL than those of the control conditions. Thus, the characteristic modification of VT duration and CL by NIF was reversed or minimized by the addition of LID.

Dynamics of Spiral Excitation

Video images of excitation during VT were analyzed in 6 hearts. Under the control conditions some form of rotors (single-loop or figure-8 re-entry) was documented in 11 episodes (61.1%) of the 18 VT available for image analysis. The remaining 7 VT showed one-way propagation of wave fronts traversing the observation area. Stable spirals lasting >5 s were recognized in 6 episodes in 11 VT with visible rotors, whereas in the remaining 5 episodes the rotors were unstable and turned into one-way propagation or were annihilated by collisions with wave fronts from other sites.

Fig 5 shows representative experiments. All data in Fig 5 were obtained from the same heart. Fig 5A illustrates the activation pattern during VT 5 s after the initiation. Counterclockwise rotation of wave fronts around a line of block (~12 mm) can be seen. The VT CL of 5 consecutive beats ranged from 138 ms to 158 ms. The line of block was concluded to be functional, because there was no appreciable conduction delay in the area during constant stimulation, and the line shifted to other sites during different VT episodes induced in the same heart.

The functional block line, which was parallel to the fiber orientation, was composed of 2 segments: a central segment with a large phase-shift between the 2 opposite limbs of the circuit, and small terminal segments with localized conduction delay[15] The circuit was more or less stable for more than 20 s and exhibited moderate meandering.

Optical action potential signals recorded around the circuit are shown at the bottom. Action potentials at sites close to the pivot points are characterized by a longer time to peak (slower upstroke) (sites 3, 4, 8). After passing through the pivot, the action potential had a shorter time to peak (faster upstroke) (site 5, 6). The action potentials recorded in the central segment of the functional block line exhibited double potentials (site 9). There were minimal isoelectric segments, which may reflect electrical diastole, between successive action potentials throughout the circuit.

Fig 5B shows an activation pattern during a short VT (lasting for 2 s) induced after application of NIF alone. Two functional block lines and distorted figure-8 circuits are recognized in the isochrone map. The upper block line was longer than 21 mm, and the circuit was unstable and meandered considerably. The VT CL of 5 consecutive beats ranged from 202 ms to 276 ms. The action potential recorded from the circuit showed appreciable beat-to-beat variation, but the basic characteristics of anisotropic reentry observed under the control conditions were preserved (a line of block parallel to fiber orientation, a longer time to peak of action potentials around the pivot point, and minimal isoelectric segment between successive action potentials). A local conduction block was recognized between sites 6 and 7, giving rise to a further extension of the functional block line. Site 7 was excited by a wave front turning around the line of the block. The rotor terminated spontaneously 2 cycles later following an extension of the functional block line in the opposite direction (site 4).

Fig 5C shows an activation pattern during a VT of longer duration (lasting for 11 s) after addition of LID (NIF+LID). Figure-8-type double loops circulating around 2 functional block lines were maintained for >5 s with moderate meandering. The VT CL of 5 consecutive beats ranged from 186 to 228 ms. The length of the 2 functional block lines was 14–16 mm and 6–8 mm, respectively. The action potentials recorded from the circuits showed less beat-to-beat variation, and the incidence of local conduction block was reduced.

Qualitatively similar results were obtained in all 6 hearts exhibiting visible rotors under control conditions. Thus, application of NIF alone caused prolongation of the functional block line, an increase in meandering of the circuit, and earlier termination of rotation. All of these effects of NIF were reversed or minimized after addition of LID (NIF+LID).

Discussion

The major findings of the present study are: (1) VT induced in isolated rabbit heart having a 2-D ventricular myocardial structure and uniform anisotropic properties were mediated by spiral-type excitation circulating around variable functional block lines, (2) NIF slowed VT CL and caused early termination due to destabilization of the spiral dynamics, and (3) addition of LID prevented the NIF action on the spiral-type re-entrant VT.

Action Potentials and Conduction Velocity

The anisotropic conduction properties of the 2-D epicardial layer of rabbit ventricles observed in the current study were consistent with those reported by Schalij et al in a similar rabbit heart model with endocardial freezing[15] In pilot experiments we measured CV and APD on the anterior epicardial surface of the left ventricular free wall in 4 intact rabbit hearts (without endocardial freezing) by using the same stimulation and optical mapping procedures as described in the present paper. Longitudinal and transverse CV (θ_L, θ_T) in the intact hearts during constant stimulation were 54.6±3.0 cm/s and 23.2±1.5 cm/s, respectively at S1–S1 400 ms, and 55.8±4.0 cm/s and 20.7±1.2 cm/s, respectively at S1–S1 250 ms. The APD90 during the constant stimulation was 179±8 ms at S1–S1 400 ms and 141±5 ms at S1–S1 250 ms. There were no substantial differences between the intact hearts and the 2-D hearts (Tables 1,2) in θ_L and APD90. The transverse CV (θ_T) in the intact hearts was slightly faster (by 4–5%) than in the 2-D hearts

(Table 1). This may be attributable to transition of the microscopic propagation mode from transverse to longitudinal at the periphery of the recording area in the intact hearts[15] These observations suggest that the basal electrophysiological properties of ventricular muscle were unaffected by the freezing procedure.

In the present study we used NIF in vitro at a concentration of 0.5 μmol/L, which approximately corresponds to the peak plasma concentration in human subjects (~0.2 mg/L)[6] At this concentration, NIF primarily suppresses the rapid activating component of the delayed rectifier potassium current (I_{Kr})[3,5,6] Nifekakant also suppresses other voltage- and ligand-gated potassium channel currents, but at much higher concentrations[4,6]

Nifekakant caused nearly uniform prolongation of APD during constant stimulation in our rabbit ventricular muscle preparations, whereas the CV along and across the fiber orientation (θ_L and θ_T) were unaffected by NIF. These effects can be interpreted by selective block of I_{Kr}. Addition of 3 μmol/L LID partially reversed the APD prolongation without affecting the CV, and this action of LID is most likely attributable to blockade of the slow component of Na current ($I_{Na,\,slow}$) during the plateau-phase action potential[17] Low concentrations of LID have been shown to suppress $I_{Na,\,slow}$[17] without affecting $I_{Na,\,fast}$, which is responsible for the upstroke phase of action potentials, a major determinant of CV in cardiac tissue. The APD of ventricular myocytes is regulated by a delicate balance between inward and outward currents, as the membrane resistance during the plateau phase is very high. Thus, the APD prolongation via reduction of I_{Kr} by NIF would be readily counteracted by a concomitant reduction of $I_{Na,\,slow}$ in response to addition of LID.

VTs of Spiral-Type Re-Entry

In the present study we used S1–S2 cross-field stimulation to induce VT of spiral-type excitations; DC field stimulation of moderate intensity (S2: 20 V) was applied during the vulnerable period of preceding excitation (S1) in a direction that crossed the ventricular propagation of S1 excitation. This stimulation protocol is known to most reliably produce a free end of the propagating wave front (wave break), and subsequent curling to produce the tip of a rotor[18] In our optical image analysis, spiral-type excitations of single or double loops circulating around functional block lines were actually induced in the observation area in more than half (61%) of all VT episodes under the control conditions. One-way propagation of wave fronts traversing the observation area in the remaining VT episodes (38%) may have arisen from invisible rotors on the opposite surface of the heart. VTs induced were polymorphic during the initial several beats, but stabilized during subsequent beats. This transition is a characteristic behavior of re-entrant VT induced in a 2-D myocardial layer with uniform anisotropy[15,19] Discontinuous anisotropic characteristics of the myocardium may set the stage for such anchoring behavior.

VTs induced in the presence of NIF alone are characterized by a longer CL and much earlier spontaneous termination than those observed in the controls. The CL of non-sustained VT was markedly prolonged (by 27%). Such modification was associated with marked destabilization of spiral dynamics documented in the optical images; greater meandering of re-entry circuits, prolongation of functional block lines and frequent occurrence of local conduction blocks.

The NIF-induced modification of spiral dynamics may be the result of a repolarization delay in the circuit. All of the action potentials in the re-entrant circuit in the spiral-type excitations during VT in the absence (control) and presence of NIF were elicited successively, with minimal isoelectric segments between excitations. The fluorescence signals do not represent absolute transmembrane potential, and their precise interpretation is hampered by low-pass space filtering. Despite such limitations, however, the action potential signal configurations around the functional block line seem to suggest minimal electrical diastole reflecting an excitable gap in the circuit. Substantial prolongation of APD in such re-entrant circuits should lead a tremendous increase in interactions between the wave-front and wave-tail[20,21] The functional block line, which is formed by the refractory wake of the wave moving in the opposite direction, has to be prolonged to maintain the rotation[20,21] The wave front would encounter its own tail more and more frequently and produce numerous local conduction blocks, giving rise to the complex meandering of the circuit[20,21] This may increase the opportunity for breakup or annihilation of the rotation.

The NIF-induced changes in VT duration, VT CL, and spiral dynamics were all partially reversed by addition of LID. This LID-induced reversal is interpreted as most likely being due to a counteracting abbreviation of APD.

Clinical Implications

In the present study, NIF and LID were applied at the beginning in the conditioning period of constant stimulation (before induction of VT). However, since in the clinical practice these drugs are usually used in patients with VT/VF, this difference in the drug application mode should be kept in mind when considering the clinical implications of our data.

In many recent model and experimental studies the investigators have postulated that spiral-type excitations (rotors) are the central organizing machinery of VF[22] Two major mechanisms for the maintenance of VF have been identified. Some investigators have proposed that VF results from the instability of rotors, which ultimately leads to their continuous breakup[23,24] while others have hypothesized that fibrillation is maintained by wave fronts emanating at an exceedingly high frequency from a relatively stable rotor[25–27] In other words, a rapidly circulating rotor (mother rotor) is the fundamental driver of VF, and the multiple wavelets that characterize VF are epiphenomena caused by fibrillatory conduction block. These 2 mechanisms are not totally incompatible, but may make complementary contributions in various heart diseases[28]

Based on the results of the present study, NIF is expected to be effective in preventing VF, if the VF is attributable to rapidly circulating mother rotors, as it destabilizes rotation activity. Failure of ventricular defibrillation by DC shocks at an energy below a certain level is mainly attributable to induction of new mother rotor-type excitations, giving rise to re-initiation of fibrillation. Administration of NIF would be effective in preventing such shock-induced re-initiation of fibrillation. In canine experiments, in fact, NIF has been shown to lower the defibrillation threshold[29] Addition of LID would antagonize these beneficial actions of NIF.

However, NIF has the ability to increase VF perpetuation, if it is due to continuous breakup of wave fronts. Addition of LID might antagonize such an undesirable action

of NIF. More extensive experimental studies are required to resolve these issues.

Study Limitations

In the current study we used a 2-D subepicardial layer of ventricular myocardium to analyze drug actions on spiral-type re-entrant arrhythmias, but the dynamics of spiral-type excitations (scrolls) in real hearts, with their 3-D structure, are much more complex.[14] Moreover, spontaneous VT/VF normally occurs in diseased hearts with a variety of functional and morphological abnormalities, not in healthy hearts.[30] We used BDM as an excitation-contraction uncoupler, but it is known to have substantial effects on the electrophysiological characteristics of cardiac myocytes.[31] Moreover, there are considerable species differences in the relative contribution of the rapidly and slowly activating components of the delayed rectifier potassium current (I_{Kr} and I_{Ks}) to the repolarization of action potentials in ventricular myocytes. The relative contribution of I_{Kr} has been shown to be much greater in rabbits than in other species (guinea pigs, dogs, and perhaps humans).[32,33] The effects of NIF on the spiral-type re-entrant VT in humans may therefore be less prominent than in rabbits. These limitations should be taken into account in the application of the observations in the present study to the treatment of VT/VF in clinical practice.

Acknowledgement

This study was supported by Grant-in-Aid for Scientific Research (A), Health and Labour Sciences Research Grants Japan Society for the promotion of Science and the Research Grant for Cardiovascular Disease (15-6) from the Ministry of Health, Labour and Walfare.

References

1. Davidenko JM. Spiral waves in the heart: Experimental demonstration of a theory. *In*: Zipes DP, Jalife JJ, editors. Cardiac Electrophysiology: From Cell to Bedside, 2nd edn. Philadelphia: WB Saunders; 1995; 478–488.
2. Jalife J. Ventricular fibrillation: Mechanisms of initiation and maintenance. *Annu Rev Physiol* 2000; **62:** 25–50.
3. Nakaya H, Tose N, Takeda Y, Kanno M. Effects of MS-551, a new class III antiarrhythmic drugs, on action potential and membrane currents in rabbit ventricular myocytes. *Br J Pharmacol* 1993; **109:** 157–163.
4. Martin DK, Nakaya Y, Wyse KR, Bursill JA, West PD, Cambell TJ. Inhibition of ATP-sensitive potassium channels in cardiac myocytes by the novel class III antiarrhythmic agent MS-551. *Pharmacol Toxicol* 1995; **77:** 65–70.
5. Cheng J, Kamiya K, Kodama I, Toyama J. Differential effects of MS-551 and E-4031 on action potential and the delayed rectifier K^+ current in rabbit ventricular myocytes. *Cardiovasc Res* 1996; **31:** 963–974.
6. Nakaya H, Uemura H. Electropharmacology of nifekalant, a new class III antiarrhythmic drug. *Cardiovasc Drug Rev* 1998; **16:** 133–144.
7. Kushida S, Ogura T, Komuro I, Nakaya H. Inhibitory effect of class III antiarrhythmic drug nifekalant on HERG channels: Mode of action. *Euro J Pharmacol* 2002; **457:** 19–27.
8. American Heart Association. Guidelines 2000 for cardiopulmonary resuscitation and emergency cardiovascular care. *Circulation* 2000; **102**(Suppl): I-1–I-384.
9. Kern KB, Halperin HR, Field J. New guidelines for cardiopulmonary resuscitation and emergency care: Changes in the management of cardiac arrest. *JAMA* 2001; **285:** 1267–1269.
10. Amino M, Yoshioka K, Usui K, Deguchi Y, Tanabe T, Inokuchi S, et al. Efficacy of nifekalant hydrochloride for life-threatening ventricular tachyarrhythmias in patients with resistance of lidocaine: A study on the patients with out-of-hospital cardiac arrest. *J Cardiol* 2003; **41:** 127–134.
11. Takenaka K, Yasuda S, Miyazaki S, Kurita T, Sutani Y, Morii I, et al. Initial experience with nifekalant hydrochrolide (MS-551), a novel class III antiarrhythmic agent, in patients with acute extensive infarction and severe ventricular dysfunction. *Jpn Circ J* 2001; **65:** 60–62.
12. Sahara M, Sagara K, Yamashita T, Iinuma H, Fu LT, Watanabe H. Nifakalant hydrochloride, a novel Class III antiarrhythmic agent, suppressed postoperative recurrent ventricular tachycardia in a patient undergoing coronary artery bypass grafting and the Dor approach. *Circ J* 2003; **67:** 712–714.
13. Myoshi M, Yasuda S, Miyazaki S, Ueno K, Morii I, Satomi K, et al. Intravenous administration of nifekalant hydrochloride for the prevention of ischemia-induced ventricular tachyarrhythmia in patients with renal failure undergoing hemodialysis. *Circ J* 2003; **67:** 898–900.
14. Pertsov AM, Jalife J. Scroll waves in three-dimensional cardiac muscle. *In*: Zipes DP, Jalife JJ, editors. Cardiac Electrophysiology: From Cell to Bedside, 3rd edn. Philadelphia: WB Saunders; 2000; 336–344.
15. Schalij MJ, Lammers WJ, Rensma PL, Allessie MA. Anisotropic conduction and reentry in perfused epicardium of rabbit left ventricle. *Am J Physiol* 1992; **263:** H1466–H1478.
16. Lee MH, Lin SF, Ohara T, Omichi C, Okuyama Y, Chudin E, et al. Effects of diacetyl monoxime and cytochalasin D on ventricular fibrillation in swine right ventricles. *Am J Physiol Heart Circ Physiol* 2001; **280:** H2689–H2696.
17. Grant AO, Whaley DW, Wendt DJ. Pharmacology of the cardiac sodium channel. *In*: Zipes DP, Jalife JJ, editors. Cardiac Electrophysiology: From Cell to Bedside, 3rd edn. Philadelphia: WB Saunders; 2000; 247133–247141.
18. Wellner M, Berenfeld O. Theory of reentry. *In*: Zipes DP, Jalife JJ, editors. Cardiac Electrophysiology: From Cell to Bedside, 4th ed. Philadelphia: WB Saunders; 2004; 317–326.
19. Schalij MJ, Boersma L, Huijberts M, Allessie MA. Anisotropic reentry in a perfused 2-dimensional layer of rabbit ventricular myocardium. *Circulation* 2000; **102:** 2650–2658.
20. Fast VG, Kleber AG. Role of wavefront curvature in propagation of cardiac impulse. *Cardiovasc Res* 1997; **33:** 258–271.
21. Beaumont J, Jalife J. Rotors and spiral waves in two dimensions. *In*: Zipes DP, Jalife JJ, editors. Cardiac Electrophysiology: From Cell to Bedside, 3rd edn. Philadelphia: WB Saunders; 2000; 327–335.
22. Samie FH, Jalife J. Mechanisms underlying ventricular tachycardia and its transition to ventricular fibrillation in the structurally normal heart. *Cardiovasc Res* 2001; **50:** 242–250.
23. Weiss JN, Garfinkel A, Karagueuzian HS, Qu Z, Chen PS. Chaos and the transition to ventricular fibrillation: A new approach to antiarrhythmic drug evaluation. *Circulation* 1999; **99:** 2819–2826.
24. Garfinkel A, Kim Y-H, Voroshilovsky O, Qu Z, Kil JR, Lee M-H, et al. Preventing ventricular fibrillation by flattening cardiac restitution. *Proc Natl Acad Sci USA* 2000; **97:** 6061–6066.
25. Chen J, Mandapati R, Berenfeld O, Skanes AC, Jalife J. High-frequency periodic sources underlie ventricular fibrillation in the isolated rabbit heart. *Circ Res* 2000; **86:** 86–93.
26. Beaumont J, Davidenko N, Davidenko JM, Jalife J. Spiral waves in two-dimensional models of ventricular muscle: Formation of a stationary core. *Biophys J* 1998; **75:** 1–14.
27. Samie FH, Berenfeld O, Anumonwo J, Mironov SF, Udassi S, Beaumont J, et al. Rectification of the background potassium current: A determinant of rotor dynamics in ventricular fibrillation. *Circ Res* 2001; **89:** 1216–1223.
28. Chen PS, Wu T-J, Ting C-T, Karagueuzian HS, Garfinkel A, Lin S-F, et al. A tale of two fibrillations. *Circulation* 2003; **108:** 2298–2303.
29. Murakawa Y, Yamashita T, Kanese Y, Omata M. Can a class III antiarrhythmic drug improve electrical defibrillation efficacy during ventricular fibrillation? *J Am Coll Cardiol* 1997; **29:** 688–692.
30. Weiss JN, Chen PS, Qu Z, Karagueuzian HS, Garfinkel A. Ventricular Fibrillation: How do we stop the waves from breaking? *Circ Res* 2000; **87:** 1103–1107.
31. Cheng Y, Li L, Nikolski V, Wallick DW, Efimov IR. Shock-induced arrhythmogenesis is enhanced by 2,3-butanedione monoxime compared with cytochalasin D. *Am J Physiol Heart Circ Physiol* 2004; **286:** H310–H318.
32. Lu Z, Kamiya K, Opthof T, Yasui K, Kodama I. Density and kinetics of I_{Kr} and I_{Ks} in guinea pig and rabbit ventricular myocytes explain different efficacy of I_{Ks} blockade at high heart rate in guinea pig and rabbit: Implications for arrhythmogenesis in humans. *Circulation* 2001; **104:** 951–956.
33. Cheng J, Kodama I. Two components of delayed rectifier K^+ current in heart: Molecular basis, functional diversity, and contribution to repolarization. *Acta Pharmacol Sin* 2004; **25:** 137–145.

Available online at www.sciencedirect.com

SCIENCE DIRECT®

Journal of Electrocardiology 38 (2005) 126–130

JOURNAL OF Electrocardiology

www.elsevier.com/locate/jelectrocard

Optical imaging of spiral waves: pharmacological modification of spiral-type excitations in a 2-dimensional layer of ventricular myocardium

Itsuo Kodama, MD[a,*], Haruo Honjo, MD[a], Mastoshi Yamazaki, MD[a], Harumichi Nakagawa, MD[a], Yuko Ishiguro, MD[a], Yusuke Okuno[a], Ichiro Sakuma, PhD[b], Kaichiro Kamiya, MD[a]

[a]*Department of Circulation, Research Institute of Environmental Medicine, Nagoya University, Nagoya, Nagoya 464-8601, Japan*
[b]*Graduate School of Engineering and Frontier Sciences, The University of Tokyo, Tokyo 113-8656, Japan*

Received 10 June 2005; accepted 10 June 2005

Abstract Differential effects of sodium channel blockers, an I_{Kr} blocker (nifekalant) and amiodarone on the spiral-type reentry, were investigated in rabbit hearts by using a high-resolution optical mapping system. Two-dimensional subepicardial layer of left ventricular myocardium with uniform anisotropy was prepared by endocardial cryoablation. During ventricular tachycardia (VT) elicited by cross-field stimulation, spiral-type excitations rotating around functional block lines (FBLs) were visualized. All the sodium channel blockers stabilized rotors; VT duration was prolonged in association with increases of FBLs and VT cycle length. The rotors in the presence of nifekalant were characterized by large meandering, long FBLs, and frequent front-tail interactions generating wave breaks. Amiodarone (acute application) increased FBLs and VT cycle length, but shortened the VT duration with minimal front-tail interaction. These results suggest that multifaceted drug action on both depolarization and repolarization may be required for the early termination of spiral-type reentry without causing breakup of rotors.

Keywords: Spiral reentry; Optical mapping; Sodium channel blockers; Nifekalant; Amiodarone; Ventricular tachycardia

1. Introduction

Spiral-type reentrant excitations (rotors) circulating around a functional obstacle is the major organization center of life-threatening ventricular tachycardia (VT) and ventricular fibrillation [1-4]. Pharmacological regulation of such rotors is therefore the central issue to be resolved for efficient prevention of sudden arrhythmic death [2-4]. As to the effects of antiarrhythmic drugs on the dynamics of spiral reentry in real hearts, however, information available is still limited and much remains to be clarified. We investigated differential effects of sodium channel blockers (pilsicainide, disopyramide, cibenzoline), a blocker of the rapid component of the delayed rectifier K^+ current (I_{Kr}) (nifekalant) [5], and amiodarone (acute application) on the spiral-type reentry in rabbit hearts by using our custom-made high-resolution optical mapping system.

2. Experimental model

In the intact heart, vortex-type excitations appear only transiently because of its 3-dimensional structure with variable filament configuration, thereby hampering detailed analysis of spiral dynamics by optical mapping. To avoid this problem, we created a 2-dimensional preparation by the method similar to those used by Schalij et al [6]. In brief, the Langendorff-perfused rabbit heart was immersed in a tissue bath containing perfusion fluid at 37°C, a cryoprobe made of copper was inserted into the left ventricular cavity, then the probe was filled with liquid nitrogen (−192°C) for 5 minutes. This freezing procedure destroyed the endocardial and intramural layers of the free wall of the left ventricle and the total interventricular

* Corresponding author. Tel.: +81 52 789 3869; fax: +81 52 789 3890.
E-mail address: ikodama@riem.nagoya-u.ac.jp (I. Kodama).

0022-0736/$ – see front matter © 2005 Elsevier Inc. All rights reserved.
doi:10.1016/j.jelectrocard.2005.06.025

septum, leaving only a thin left ventricular epicardial layer intact. The thickness of surviving myocardium was 1.0 ± 0.2 mm (10 hearts).

3. Optical mapping procedures

The optical mapping procedure in this series of experiments was essentially the same as described in our previous report [7]. In brief, the hearts (after endocardial freezing) were stained with the voltage-sensitive dye di-4-ANEPPS (Molecular Probes, Eugene, Ore), and their mechanical contraction was minimized by adding a 2,3-butanedione monoxime concentration of 15 mmol/L. The vertically hanging heart placed in the Langendorff apparatus was illuminated with bluish light-emitting diodes mounted on a ring-shaped bracket placed in front of the heart. The wavelength of excitation light was 505 ± 20 nm. The fluorescence emitted from the epicardial surface of the heart was recorded by a high-speed digital video camera (Fastcam-Ultima 40K or Fastcam-Max, Photron, Tokyo, Japan). This solid-state image-sensing device camera was used to acquire 5-bit or 10-bit gray scale images from 256 × 256 sites simultaneously at a speed of 750 to 1000 frames per second. A long-pass glass filter (cutoff wavelength, 600 nm) was mounted on the camera. The images acquired (30 × 30 mm) covered the anterolateral surface of the left ventricle, yielding a spatial resolution of 0.12 mm per pixel. The digital images were stored temporarily in the frame memory and then transferred to a personal computer for off-line analysis.

The fluorescence signals were spatially averaged to reduce noise. The data from 3 × 3 pixels were averaged to obtain isochrone maps, whereas the data from 4 × 4 pixels were averaged to analyze action potential configuration. The front-tail dynamics during VT was visualized by connecting the 10% depolarization points in the action potential upstrokes as the wave front in the recording area and by connecting the 90% repolarization points as the wave tail. We quantified the pattern of wave propagation during VT using phase mapping method reported by Gray et al [1].

4. Anisotropic conduction properties

In the experiments, to see the conduction velocity and the action potential configuration under constant stimulation, basic (S1) stimuli were applied to an anterior center of the left ventricle at cycle length of 220 to 800 milliseconds. The activation front always showed a smooth and symmetric elliptical pattern; the long axis of the ellipse corresponded to the fiber orientation of subepicardial cardiac muscle, indicating uniform anisotropy in the observation area [7]. The conduction velocities in longitudinal and transverse propagation under the control conditions were 48 to 56 and 20 to 23 cm/s, respectively. The anisotropic ratio of the velocity was 2.5 to 2.8.

5. Ventricular tachycardia and spiral-type excitation

In the experiments, to induce VT resulting from spiral-type excitation, 18 S1 stimuli at cycle length of 400 milliseconds were applied to the apex, and then a 10-millisecond direct current stimulus (S2, monophasic pulse at 20 V) was delivered through a pair of paddle electrodes (5 to 7-mm-diameter) placed on the lateral surface of both ventricles. This cross-field stimulation was applied during the vulnerable window of the last S1 excitation. Under the drug-free control conditions, 116 VTs were induced in 29 hearts. In the video images of fluorescence signals, certain forms of rotors (single loop or figure-of-8 reentry) were documented in 61 VTs (53%). The remaining 55 VTs showed 1-way propagation of wave fronts traversing the observation area.

Fig. 1 shows a representative experiment. In the isochrone map (left), clockwise rotation of wave fronts around a line of block (2.4 mm) with a VT cycle length of 115 to 118 milliseconds can be seen. The line of block was concluded to be functional, because there was no appreciable conduction delay in the area under constant stimulation. In addition, the line moved to other sites during different VT episodes in the same heart. The functional block line (FBL) was composed of 2 segments: a central segment with a large phase shift between the 2 opposite limbs of the circuit and small terminal segments with localized conduction delay. The circuit was more or less stable for longer than 10 seconds and exhibited moderate meandering. Optical action potential signals at sites close to the pivot points were characterized by a longer time to peak (slower upstroke). The signals recorded at the center of the FBL exhibited low-amplitude double potentials. There were minimal isoelectric segments, which may reflect electrical diastole, between successive action potentials throughout the circuit.

6. Effects of sodium channel blockers

Under basic stimulation, a 20-minute application of a pilsicainide concentration of 5 μmol/L [8] resulted in a decrease of conduction velocity by 30% to 40% with no substantial changes in action potential duration (APD). Ventricular tachycardias induced by S1-S2 cross-field stimulation in the presence of pilsicainide had slower rate and longer duration than the control. Ventricular tachycardia cycle length was increased from 152 ± 5 milliseconds in the control to 241 ± 34 milliseconds after pilsicainide ($n = 10$, $P < .05$). The incidence of sustained VT (>30 seconds) was increased from 21% (4/19) to 57% (12/21).

Fig. 2A shows a single spiral induced after application of pilsicainide. Wave fronts are circulating around the FBL that is much longer than the control especially at their terminal segments parallel to the fiber orientation. The VT cycle length was prolonged from 205 to 210 milliseconds, and the VT lasted longer than 30 seconds. In the action potential

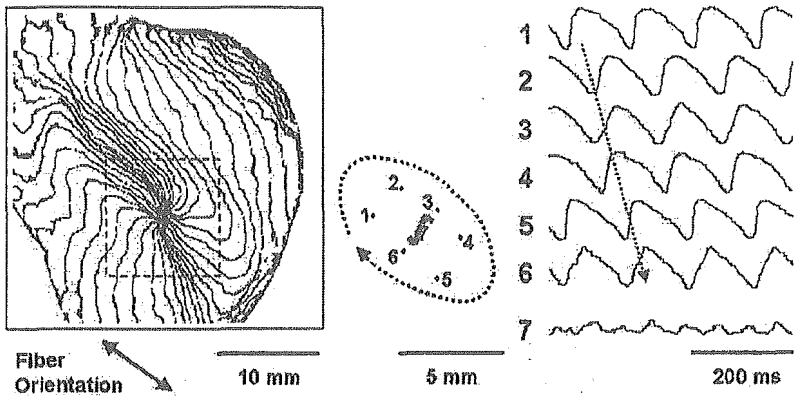

Fig. 1. Isochrone map of activation during VT induced by cross-field stimulation under the control condition. The isochrone interval was 4 milliseconds. A thick lines indicate FBLs. The cycle length of ventricular excitation was 115 to 118 milliseconds. Sequential records of optical action potential signals from 7 sites in the circuit are shown on the right.

signals around the circuit, substantial isoelectric segments (electrical diastole) are visible at sites before entering and after passing the pivot points.

Qualitatively similar results were obtained for disopyramide (30 μmol/L) and cibenzoline (3 μmol/L). The effects of sodium channel blockers are therefore summarized as follows: (1) The FBL is prolonged because longer wave fronts are required for turning around the pivot points across the fibers. (2) sodium channel blockers cause substantial electrical diastole (corresponding to excitable gap) in the circuit except at sites around the pivot points. (3) Reentry (VT) cycle length is markedly prolonged. (4) The spiral-type excitation is more stabilized and lasts longer than the control.

7. Effects of nifekalant

Under basic stimulation, a 20-minute application of a nifekalant concentration of 0.1 μmol/L caused a prolongation of APD by 7% to 25% without affecting the conduction velocity. This APD prolongation was greater at longer cycle length. Ventricular tachycardias induced by S1-S2 cross-field stimulation in the presence of nifekalant had longer cycle length and shorter duration than the

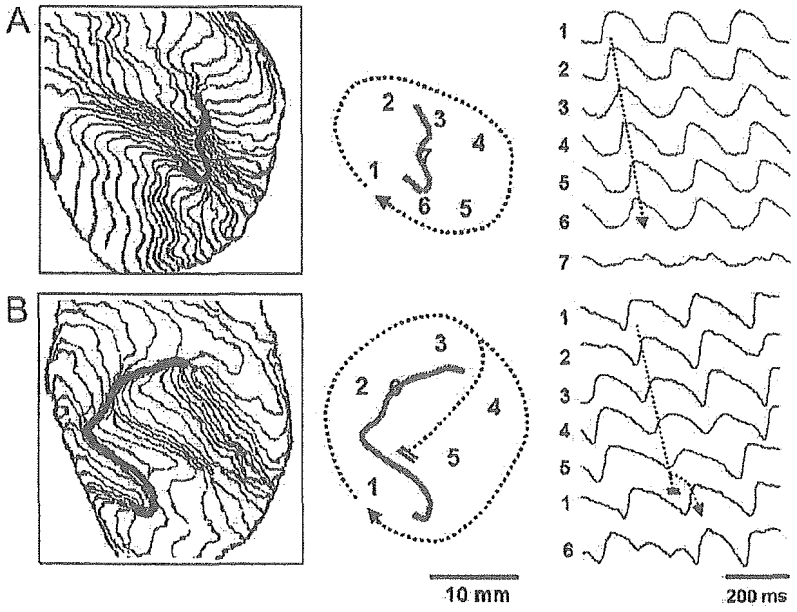

Fig. 2. A, Isochrone map of activation during VT induced by cross-field stimulation after application of a pilsicainide concentration of 5 μmol/L. B, Isochrone map of activation during VT induced after a nifekalant concentration of 0.1 μmol/L. The isochrones were drawn every 4 milliseconds. Thick lines indicate FBLs. Sequential records of optical action potential signals in the respective circuit are shown on the right. Ventricular tachycardia cycle lengths were 132 to 133 milliseconds for pilsicainide and 169 to 190 milliseconds for nifekalant.